
Article:
McDermott, S., Li, P., Williams, G. et al. (1 more author) (2017) Characterizing a spatial light modulator using ptychography. Optics Letters, 42 (3). pp. 371-374. ISSN 0146-9592

https://doi.org/10.1364/OL.42.000371

Characterising a Spatial Light Modulator using Ptychography

SAMUEL MCDERMOTT[1,*], PENG LI[1], GAVIN WILLIAMS[1], AND ANDREW MAIDEN[1]

[1] Department of Electronic and Electrical Engineering, University of Sheffield, Sheffield, S1 4DE, UK
[*] Corresponding author: smcdermott1@sheffield.ac.uk

Compiled December 11, 2016

Ptychography is used to characterise the phase response of a Spatial Light Modulator (SLM). We use the technique to measure and correct the optical curvature and the gamma curve of the device. Ptychography's unique ability to extend field-of-view is then employed to test performance by mapping the phase profile generated by a test image to sub-pixel resolution over the entire active region of the SLM.

OCIS codes: *070.6120 100.5070*

http://dx.doi.org/10.1364/ao.XX.XXXXXX

In recent years, phase-only Spatial Light Modulators (SLMs) have become a popular way to shape light in a range of applications, from holographic displays [1] to structured illumination microscopy [2] and quantitative phase imaging [3]. The ideal phase-only SLM operates as an addressable phase mask that can program an arbitrary profile onto a coherent beam; in practice, the degree of control is limited by the SLM's physical properties: its pixel fill factor, number of quantisation levels, the imprecise mapping of voltages onto phase shifts, and optical distortions such as the curvature of the device's surface. Characterising these features is an important step toward successfully incorporating an SLM into an optical system, and a number of characterisation techniques have been demonstrated previously. Examples include using a Mach-Zehnder interferometer [4], a Twyman-Green interferometer [5], and digital holography [6]. A grating-based instrument has been used to obtain a large field-of-view (FoV) phase image of an SLM [7], but only at a resolution limited by the system's NA of 0.0075. Conversely, Kohler *et al.* employed a novel phase retrieval algorithm to characterise an SLM [8], obtaining sub-pixel-resolution phase images of the device, but only over a small FoV.

Some of the approaches described above are aimed exclusively at extracting the phase response of the SLM, outputting a plot of the average phase change the device produces at each phase level that it can be programmed to display. Those that image the SLM either do so over small areas or over large areas at low resolution. All of the methods are susceptible to errors resulting from imperfect optical components in the characterization setup, and those based on interference with a reference beam involve careful alignment and calibration. In this paper we use ptychography [9]–with its ability to realise precise, high resolution phase images over extremely large FoV–to overcome these drawbacks.

For those unfamiliar with ptychography, the concept is as follows. A localized coherent 'probe' beam illuminates a small region of a specimen. The specimen is translated laterally relative to the beam through a discrete grid of positions, so that the set of illuminated areas together form an overlapping patchwork that covers a region of interest. At each specimen position a diffraction pattern is recorded by a detector placed some distance downstream. The overlap between the areas illuminated by the probe allows iterative algorithms to solve the inverse problem of determining the complex transmissivity or reflectivity of the specimen, and the probe wavefront, that must have given rise to the recorded data.

Our setup to implement a reflection-mode, lens-free imaging version of ptychography is shown in Figure 1 (and see [10]). To form the probe, a 675 nm laser was coupled through a single-mode fibre and polarised along the long axis of our Liquid Crystal on Silicon (LCoS) phase-only SLM to align with its liquid crystal orientation. The beam was then passed through a weak diffuser (to reduce internal reflections in our setup) and brought to a focus by a lens. The specimen was positioned slightly downstream of the beam's tightest focal point, where the probe's diameter was 1 mm. This was the maximum size allowed by the need to sample intensity fringes in the diffraction data above the Nyquist rate. (Note that randomizing the probe by introducing a diffuser does not compromise the reconstructed specimen image, since ptychographic algorithms solve for the probe and remove its influence.) The scattered probe reflected from the specimen was directed onto an Allied Vision Pike 16-bit CCD detector (2048 × 2048 pixels on a 7.4 µm pitch) via a non-polarising beam-splitter. The NA of our lensless imaging system was kept as large as possible by minimizing the distance between the specimen and the detector; after correcting for the refractive index of the beam-splitter, this resulted in an effective camera length of 4.6 cm and an NA of 0.16, corresponding to an expected resolution in our reconstructed images of approximately 2.8 µm (by Sparrow's criterion [11]).

In each of our experiments the specimen, either a test sample or the SLM itself, was translated by a Newport XPS-Q4 x-y translation stage through a rectangular grid of positions with a pitch of 200 µm. To avoid reconstruction artefacts associated with a perfectly regular translation grid [12], random x/y offsets within the range ±40 µm were added to each position. At each

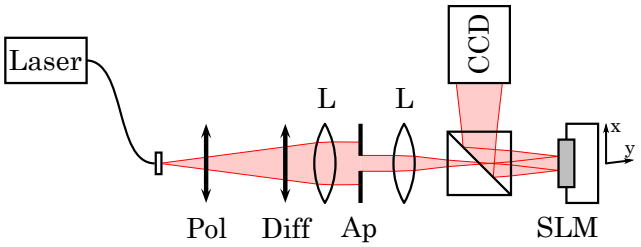

Fig. 1. The experimental setup for observing an SLM using ptychography. The SLM is mounted on a mechanical x-y stage and moves independently to the rest of the components. (Pol = linear polariser; Diff = weak diffuser; Ap = circular aperture; L = lens, focal length = 75mm).

position in the grid, a diffraction pattern was recorded with a detector binning of two and an exposure time of 1.8 s. These lengthy exposures helped average out phase flicker–a problem of phase-modulating SLMs [13]–from our final reconstructions, although they did have the side-effect of prolonging data collection for our larger scan patterns to over an hour. This and the long reconstruction time for larger scans (several hours) are the main weaknesses of our method in comparison to the alternatives, so an interesting follow up to this work would be to significantly improve data collection time using multi-mode ptychographic reconstruction [14].

The SLM we used was a Holoeye PLUTO. This is a reflective, phase-only LCoS device with 1920×1080 pixels on a pitch of 8.0 µm, and a fill-factor of 90%. The phase of each pixel can be programmed to 256 phase levels $(0-255)$, with full 2π operation possible up to a wavelength of 800 nm.

Images were reconstructed from diffraction data using the ePIE approach with the addition of position correction [15]–a necessary inclusion because the large translations involved in our extended FoV experiments caused backlash positioning errors of the order of 20 µm. We also modified the standard 'modulus constraint' in our reconstruction algorithm to account for background noise (resulting from detector readout and stray light) and for an unmodulated reflection from the SLM.

The ePIE begins with arbitrary initial estimates of the specimen and of the probe beam, then uses each recorded diffraction pattern in turn to update them. During each update step, the current estimates of the probe and specimen are used to predict the wavefront, $\psi_{\mathbf{u}}$, that was incident at the detector when the diffraction pattern intensity currently under consideration, $I_{\mathbf{u}}$, was recorded. ($\mathbf{u} = [j,k]$ indexes the pixels of the detector.) The modulus constraint refines the predicted wavefront to agree with the measured data by replacing its modulus with $\sqrt{I_{\mathbf{u}}}$ whilst leaving its phase unchanged. This revised wavefront is propagated back to the specimen plane where it is used to update the probe and specimen estimates, before moving on to consider the next diffraction pattern. The algorithm terminates when a prescribed error level is reached or, as here, after a predetermined number of iterations have been completed–more detail can be found in [15]. To include a background signal, $B_{\mathbf{u}}$, in this update step, we adopt an approach similar to that of multi-mode ptychography, revising the modulus constraint according to equation 1:

$$\psi'_{\mathbf{u}} = \psi_{\mathbf{u}} \sqrt{\frac{I_{\mathbf{u}}}{|\psi_{\mathbf{u}}|^2 + B_{\mathbf{u}}}} \qquad \textbf{(1)}$$

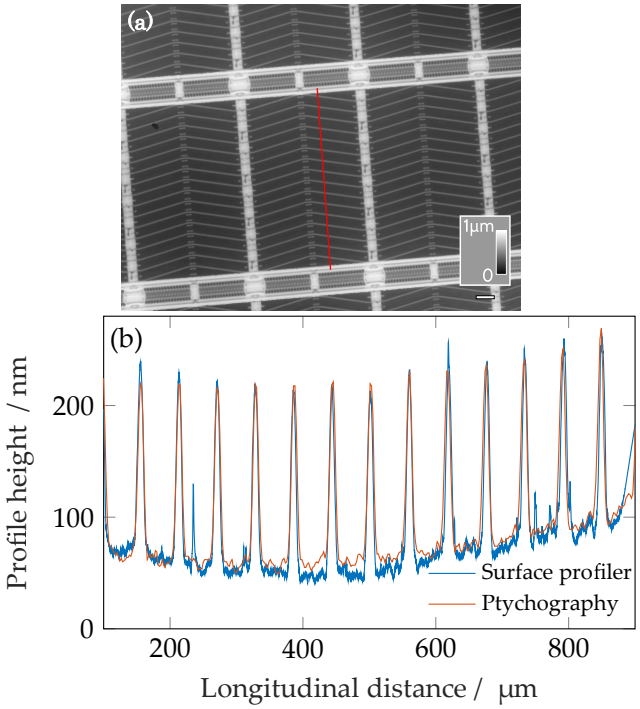

Fig. 2. Comparison of ptychographical reconstruction and surface profile of a silicon chip. (a) Ptychographic phase reconstruction of the silicon chip. The red line indicates the approximate location of the cross-section through the sample. Scale bar 0.1mm. (b) Comparison of profile heights from the surface profiler and ptychography.

where the prime denotes the updated wavefront. This assumes a model for our recorded diffraction pattern that is the incoherent sum of the wavefront propagated from the SLM and a background that does not change from recording to recording. We begin with a constant-valued estimate for $B_{\mathbf{u}}$ then update it along with $\psi_{\mathbf{u}}$ using equation 2:

$$B'_{\mathbf{u}} = B_{\mathbf{u}} \left((1-\delta) + \delta \frac{I_{\mathbf{u}}}{|\psi_{\mathbf{u}}|^2 + B_{\mathbf{u}}} \right) \qquad \textbf{(2)}$$

Here δ is an adjustable constant that governs the update rate; it was set to 0.01 in the reconstructions undertaken for this work. $B_{\mathbf{u}}$ was initialised to 5000 counts at every pixel, or around 10% of the maximum pixel value in $I_{\mathbf{u}}$.

We have found this background correction approach works well with simulated data, and it visibly improves our reconstructions here by reducing noise and reflection-like artefacts that we attribute to the unmodulated polarisation state in the illumination.

The accuracy of phase images reconstructed by ptychography is now well-established, e.g. [16]. To reinforce this previous work and to establish the accuracy of our reflection-mode experiments, we used a gold-covered silicon chip, originally part of a CMOS image sensor, as a calibration sample. The chip was mounted on the x-y stage in place of the SLM, 225 diffraction patterns over a 15×15 position grid were recorded as detailed above, the data fed to the ePIE, and after 300 iterations of the algorithm the image shown in Figure 2a was obtained (the phase has been mapped to feature height). A cross-section of the surface features on the chip was then measured using a diamond stylus profiler and compared to data taken from approximately the

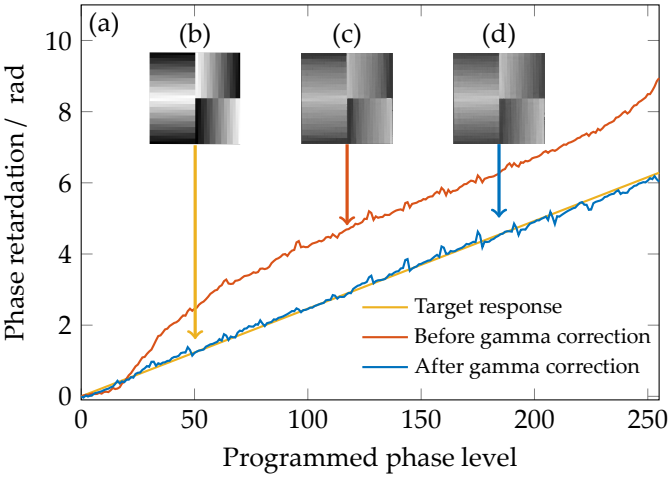

Fig. 3. The phase response of the SLM before and after gamma correction. (a) Plots of the phase responses before and after correction. (b) Test pattern used for phase characterisation of the SLM. (c) Reconstructed phase of the SLM before gamma correction, with the red line its quantitative response. (d) Reconstructed phase of the SLM after gamma correction, with its blue line close to the yellow target response.

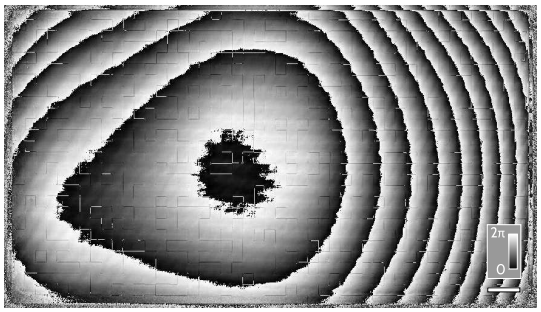

Fig. 4. A simple line patterned displayed on the SLM shows spherical deformity when reconstructed with ptychography. Scale bar 1 mm.

same position in Figure 2a, as indicated by the line. Figure 2b plots the profiles and shows that the two techniques agree on the specimen's feature heights to within 4% or <10 nm, a good match given that it was necessary to manually determine the location in the phase image from which the stylus profile was taken.

As the molecular alignment (and hence phase response) of the SLM's liquid crystal display does not react linearly to an applied voltage, the target phase image is mapped to a set of voltages via a look-up table–or gamma curve–loaded onto the SLM driver unit [17]. A necessary step in optimizing the performance of the SLM is, therefore, to adjust the gamma curve to provide a linear phase response over a $0-2\pi$ range at the wavelength of the illuminating beam [18], as indicated by the target response line in Figure 3a. To accomplish this, we set the SLM output to display at its centre the pattern of four grids shown in Figure 3b. Each grid constituted a 16×16 array of single-phase-level blocks, each of 16×16 SLM pixels, with assigned phases that stepped through the full range of programmable phase levels, from $0-255$. The four grids were flipped and rotated relative to each other so that blocks with the same programmed phase-level were not symmetrically arranged around the SLM centre–averaging blocks with the same programmed phase thereby compensated for a background curvature in the reconstructed phase image (discussed below). A set of diffraction patterns was collected and a reconstruction carried out as for the calibration sample, resulting in the image shown in Figure 3c; extracting the mean phase levels of the blocks from this image and plotting against the programmed phases clearly shows that the default gamma curve produces a non-linear phase response. (The regular kinks in the plot result from the curvature of the device surface, the effect of which was not completely removed by our flip and rotation strategy.) We computed a best fit from the phase response plot and used it to produce a revised look-up table aimed at linearising the response. This was loaded onto the SLM and a repeat of the ptychographic scan and reconstruction produced Figure 3d. Plotting the mean phase levels extracted from this image shows successful linearisation of the phase response over the required $0-2\pi$ phase range.

A further issue with SLMs results from finite manufacturing tolerances, which lead to a slight curvature across the face of the device. According to the manufacturer of our SLM, this deformation can be considered spherical and results in not more than a few microns height difference between the centre and edges [17]. Our second calibration step involved measuring this curvature and correcting for it by adding a compensating phase onto images displayed by the device. To accomplish the measurement the SLM was loaded with a pattern consisting of random one-pixel-wide, π phase-level lines covering the whole display, which gave sufficient structure to the diffraction data to condition the inverse problem solved by the reconstruction algorithm. Upon reconstruction (using the same routine as previously) we obtained the image shown in Figure 4, where the spherical deformation can be seen and a shallow phase ramp is also apparent. This ramp could have resulted from a number of sources: there is the possibility that it is an artefact of the reconstruction, it could arise from a misalignment of the optical axis and the detector, or it could be from a slight tilt to the SLM mount [19]. To compensate, we applied a counter ramp to the reconstruction before measuring the radius of each of the phase rings, from which the curvature of the device surface, R, was calculated from equation 3:

$$R = \frac{r^2 + \left(\frac{n\lambda}{2}\right)^2}{n\lambda} \tag{3}$$

where r is the radius of a 2π-phase wrap in the reconstruction, n is the order of that wrap, and λ is the wavelength of light used. Averaging over several wraps, we extracted a radius of curvature of 7.9 m, which corresponds to a maximum height discrepancy of 4.9 µm between the edge and centre of the SLM.

To test the performance of our SLM, and the effectiveness of our calibration, we carried out a ptychographic scan over the whole device area whilst it displayed a static HD phase image (inset of Figure 5). The gamma curve derived from Figure 3 was loaded onto the device driver and a spherical phase mask, of opposite sign to that measured in the calibration step, was added to the displayed image to compensate for the surface curvature (Figure 5). We collected a set of 2800 diffraction patterns, over a randomly disturbed grid of 70×40 stage translations, giving a total FoV of $9 \times 15\,\mathrm{mm}^2$. 300 iterations of the ePIE were used to reconstruct a phase image from the diffraction data, with the inclusion of position correction and the background compensation scheme detailed above.

Fig. 5. The curvature correction added to an image before display on the SLM. The inset shows the original image.

Fig. 6. The phase of the reconstructed image of the SLM, with the phase range clipped to aid contrast. The inset shows a zoom where the pixel grid of the SLM can be seen. Scale bar 1 mm.

Figure 6 shows the resulting (unwrapped) phase image. The pixel pitch in the reconstruction is 2.04 µm, and the image contains 4500×7500 pixels. The spherical correction has created a reasonably flat background to the image, but some distortion remains: a low spatial frequency ripple, around a wavelength in amplitude, which together with small unwrap errors accounts for the extension of the phase range beyond 2π. The concentric rings visible in the image correspond to phase wraps in the profile used to compensate for the SLM's surface curvature, since the strong scatter from these phase edges goes beyond the NA of our imaging system. The inset of Figure 6 shows a zoom that demonstrates the sub-pixel resolution of our final image, with each pixel of the SLM corresponding to approximately 16 pixels in the reconstruction (a slight moiré effect is present because our image pixel pitch is not an exact multiple of the SLM pitch). In the centre of the frame, the reconstruction shows excellent agreement with the intended phase profile: the programmed image had a phase difference between the light and dark stripes on the lighthouse building of 1.89 rad, calculated by averaging over a region on each stripe, whilst the difference in the same regions of the reconstructed phase was 1.91 rad.

We have demonstrated in this paper that ptychography is an excellent tool for the characterization of optical components. Its advantages include an essentially unlimited FoV, obtainable even at high image resolutions; an easy experimental setup, without need for a reference arm or imaging lenses; excellent phase accuracy; and the ability to algorithmically remove the illumination system's influence from the reconstructed image, along with any aberrations or artefacts that it may introduce.

REFERENCES

1. P. L. Makowski, T. Kozacki, P. Zdankowski, and W. Zaperty, Applied Optics **54**, 3658 (2015).
2. R. Förster, H.-W. Lu-Walther, A. Jost, M. Kielhorn, K. Wicker, and R. Heintzmann, Optics Express **22**, 20663 (2014).
3. C. Falldorf, M. Agour, C. v. Kopylow, and R. B. Bergmann, Applied Optics **49**, 1826 (2010).
4. A. Bergeron, J. Gauvin, F. Gagnon, D. Gingras, H. H. Arsenault, and M. Doucet, Applied Optics **34**, 5133 (1995).
5. H. Zhang, J. Zhang, and L. Wu, Measurement Science and Technology **18**, 1724 (2007).
6. S. Panezai, D. Wang, J. Zhao, and Y. Wang, Proceedings of SPIE **8420**, 84200F (2012).
7. G. Rajshekhar, B. Bhaduri, C. Edwards, R. Zhou, L. L. Goddard, and G. Popescu, Optics Express **22**, 3432 (2014).
8. C. Kohler, F. Zhang, and W. Osten, Applied Optics **48**, 4003 (2009).
9. A. M. Maiden and J. M. Rodenburg, Ultramicroscopy **109**, 1256 (2009).
10. D. Claus, D. J. Robinson, D. G. Chetwynd, Y. Shuo, W. T. Pike, J. J. De J Toriz Garcia, and J. M. Rodenburg, Journal of Optics **15**, 035702 (2013).
11. G. O. Reynolds, J. B. Develis, and B. Thompson, *The new physical optics notebook: tutorials in Fourier optics*, vol. 61 (American Institute of Physics, 1989).
12. M. Dierolf, P. Thibault, A. Menzel, C. M. Kewish, K. Jefimovs, U. Schlichting, K. Von König, O. Bunk, and F. Pfeiffer, New Journal of Physics **12** (2010).
13. J. García-Márquez, V. López, A. González-Vega, and E. Noé, Optics Express **20**, 8431 (2012).
14. P. Li, T. Edo, D. Batey, J. Rodenburg, and A. Maiden, Optics Express **24**, 9038 (2016).
15. A. M. Maiden, M. J. Humphry, M. C. Sarahan, B. Kraus, and J. M. Rodenburg, Ultramicroscopy **120**, 64 (2012).
16. T. M. Godden, A. Muñiz-Piniella, J. D. Claverley, A. Yacoot, and M. J. Humphry, Optics Express **24**, 7679 (2016).
17. Holoeye, *PLUTO Device Operating Instructions* (2011).
18. A. Lizana, A. Marquez, I. Moreno, C. Iemmi, J. Campos, and M. J. Yzuel, Journal of the European Optical Society: Rapid Publications **3**, 08012 (2008).
19. M. Guizar-Sicairos, I. Johnson, A. Diaz, M. Holler, P. Karvinen, H.-C. Stadler, R. Dinapoli, O. Bunk, and A. Menzel, Optics Express **22**, 14859 (2014).

FULL REFERENCES

1. P. L. Makowski, T. Kozacki, P. Zdankowski, and W. Zaperty, "Synthetic aperture Fourier holography for wide-angle holographic display of real scenes", Applied Optics **54**, 3658 (2015).
2. R. Förster, H.-W. Lu-Walther, A. Jost, M. Kielhorn, K. Wicker, and R. Heintzmann, "Simple structured illumination microscope setup with high acquisition speed by using a spatial light modulator", Optics Express **22**, 20663 (2014).
3. C. Falldorf, M. Agour, C. v. Kopylow, and R. B. Bergmann, "Phase retrieval by means of a spatial light modulator in the Fourier domain of an imaging system", Applied Optics **49**, 1826 (2010).
4. A. Bergeron, J. Gauvin, F. Gagnon, D. Gingras, H. H. Arsenault, and M. Doucet, "Phase calibration and applications of a liquid-crystal spatial light modulator", Applied Optics **34**, 5133 (1995).
5. H. Zhang, J. Zhang, and L. Wu, "Evaluation of phase-only liquid crystal spatial light modulator for phase modulation performance using a Twyman–Green interferometer", Measurement Science and Technology **18**, 1724 (2007).
6. S. Panezai, D. Wang, J. Zhao, and Y. Wang, "Study of the modulation characterization of phase-only liquid crystal spatial light modulator by digital holography", Proceedings of SPIE **8420**, 84200F (2012).
7. G. Rajshekhar, B. Bhaduri, C. Edwards, R. Zhou, L. L. Goddard, and G. Popescu, "Nanoscale topography and spatial light modulator characterization using wide-field quantitative phase imaging", Optics Express **22**, 3432 (2014).
8. C. Kohler, F. Zhang, and W. Osten, "Characterization of a spatial light modulator and its application in phase retrieval", Applied Optics **48**, 4003 (2009).
9. A. M. Maiden and J. M. Rodenburg, "An improved ptychographical phase retrieval algorithm for diffractive imaging", Ultramicroscopy **109**, 1256 (2009).
10. D. Claus, D. J. Robinson, D. G. Chetwynd, Y. Shuo, W. T. Pike, J. J. De J Toriz Garcia, and J. M. Rodenburg, "Dual wavelength optical metrology using ptychography", Journal of Optics **15**, 035702 (2013).
11. G. O. Reynolds, J. B. Develis, and B. Thompson, *The new physical optics notebook: tutorials in Fourier optics*, vol. 61 (American Institute of Physics, 1989).
12. M. Dierolf, P. Thibault, A. Menzel, C. M. Kewish, K. Jefimovs, U. Schlichting, K. Von König, O. Bunk, and F. Pfeiffer, "Ptychographic coherent diffractive imaging of weakly scattering specimens", New Journal of Physics **12** (2010).
13. J. García-Márquez, V. López, A. González-Vega, and E. Noé, "Flicker minimization in an LCoS spatial light modulator", Optics Express **20**, 8431 (2012).
14. P. Li, T. Edo, D. Batey, J. Rodenburg, and A. Maiden, "Breaking ambiguities in mixed state ptychography", Optics Express **24**, 9038 (2016).
15. A. M. Maiden, M. J. Humphry, M. C. Sarahan, B. Kraus, and J. M. Rodenburg, "An annealing algorithm to correct positioning errors in ptychography", Ultramicroscopy **120**, 64 (2012).
16. T. M. Godden, A. Muñiz-Piniella, J. D. Claverley, A. Yacoot, and M. J. Humphry, "Phase calibration target for quantitative phase imaging with ptychography", Optics Express **24**, 7679 (2016).
17. Holoeye, *PLUTO Device Operating Instructions* (2011).
18. A. Lizana, A. Marquez, I. Moreno, C. Iemmi, J. Campos, and M. J. Yzuel, "Wavelength dependence of polarimetric and phase-shift characterization of a liquid crystal on silicon display", Journal of the European Optical Society: Rapid Publications **3**, 08012 (2008).
19. M. Guizar-Sicairos, I. Johnson, A. Diaz, M. Holler, P. Karvinen, H.-C. Stadler, R. Dinapoli, O. Bunk, and A. Menzel, "High-throughput ptychography using Eiger: scanning X-ray nano-imaging of extended regions", Optics Express **22**, 14859 (2014).